

Magnetically Levitated Linear Stage with Linear Bearingless Slice Hysteresis Motors

Lei Zhou, *Member, IEEE* and David L. Trumper, *Member, IEEE*

Abstract—This paper presents the design, construction, modeling, and testing of a novel magnetically-levitated linear stage using a linear bearingless slice motor design, targeting in-vacuum transportation tasks in precision manufacturing systems. The stage is driven by novel linear hysteresis motors, where the motor secondaries are made of magnetically semi-hard material exhibiting magnetic hysteresis. The suspension of the stage in three degrees of freedom (DOFs), including vertical, pitch, and roll, is achieved passively through permanent magnet bias flux. The suspension in the lateral and yaw-directions is actively controlled. This compact design effectively reduces the number of sensors and actuators needed for stabilizing the levitation. The prototype stage has been successfully levitated with a maximum thrust force of 5.8 N under 2.5 A current amplitude, which generates a stage acceleration of 1200 mm/s². The stage position control loop has a bandwidth of 30 Hz. The stage is tested to track a reference trajectory of the target application, and the maximum position tracking error is 50 μm. The stage's lateral displacement during motion is below 50 μm, which is well below making mechanical contact to the side walls. To our knowledge, this work presents the first linear bearingless slice motor design, and also the first study on linear versions of hysteresis motors.

Index Terms—Linear motors, hysteresis motors, magnetic levitation, control system.

I. INTRODUCTION

An increasing number of semiconductor manufacturing applications require in-vacuum transportation of delicate workpieces in ultra-clean conditions. An important example is the reticle transportation in extreme ultraviolet (EUV) photolithography scanners. In the EUV photolithography process, the reticle is a 6-inch-by-6-inch reflective mask that contains a pattern defining a layer of an integrated circuit. The reticles need to be transported between a storage position and the reticle scanning stage in a clean vacuum environment via a long-stroke single-axis motion system [1]. In next-generation EUV lithography scanners, the design for such a reticle transportation system is challenging, since it needs to be vacuum compatible, satisfy a tight height constraint of below 100 mm, and with no moving mechanical contact in order to prevent particle generation.

Magnetically-levitated linear stages can be an effective solution for such in-cleanroom, in-vacuum transportation

applications, since they are compatible with the clean vacuum environment without risking contamination through mechanical contacts or air bearings. Through the years, a number of research efforts have studied designs for magnetically-levitated linear and planar motion stages, which can be roughly categorized into three groups according to their driving principles: permanent-magnet-motor-driven stages [2]–[6], induction-motor-driven stages [7], [8], and variable-reluctance-motor-driven stages [9], [10]. However, almost all these stages have limitations that may harm their performance for in-vacuum transportation. In permanent magnet (PM) motors, the PMs on the moving stage can out-gas in vacuum and thus need to be encapsulated [11], which requires a relatively complicated secondary design. Induction motors have inevitable secondary losses due to the induced currents, which is not favorable for in-vacuum operation, where cooling for the moving stage is challenging. Variable reluctance motors typically have relatively large normal and shear force ripples, which may lead to undesirable stage oscillations.

Aiming at the reticle handling application in EUV lithography scanners, in this work we present a new concept of magnetically-levitated linear stage driven by linear hysteresis motors. Hysteresis motors have secondaries made of solid and magnetically semi-hard material, and the magnetic hysteresis effect of the secondary material is used for thrust force/torque generation [12]. These motors are favorable for the proposed application for the following reasons: First, the secondary of hysteresis motors does not require any PM, which allows for a simple stage design without encapsulation needed. Second, hysteresis motors allow synchronous operation, where the fundamental harmonic excitation does not generate secondary loss, which is advantageous for thermal management. Third, hysteresis motors typically generate reduced force ripples compared with reluctance motors, which allows a relatively quiet operation. Finally, the hysteresis secondaries have high mechanical stiffness, which is beneficial for structural purposes. These advantages of hysteresis motors provide the motivation for our study of their use in linear stages. The main disadvantage of linear hysteresis motors is that their thrust force production capability is relatively low compared with other motor types. However, this is acceptable for the reticle transportation stage, since its acceleration requirement is relatively low (500 mm/s²), which is achievable with linear hysteresis motors. In the past, almost all developed hysteresis motors are in rotary form and operate in open-loop. Recent work [13] studied the closed-loop position control for rotary hysteresis mo-

L. Zhou is with the Dept. of Mechanical Engineering, The University of Texas at Austin, Austin, TX, USA. lzhou@utexas.edu.

D. Trumper is with the Dept. of Mechanical Engineering, Massachusetts Institute of Technology, Cambridge, MA, USA. trumper@mit.edu

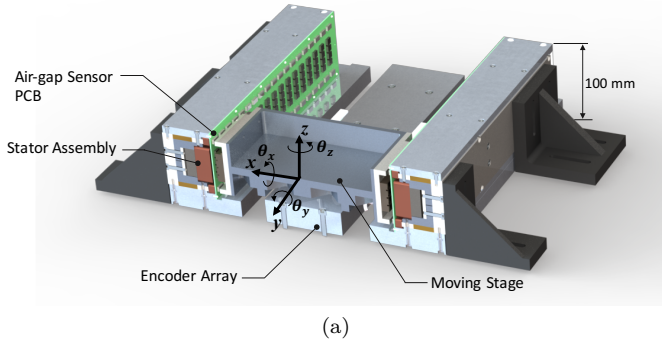


Fig. 1. (a) Cross-section CAD model of the magnetically-levitated linear stage system. (b) Photograph of the magnetically-levitated linear stage prototype.

tors. To our knowledge, our linear stage described in this paper presents the first study of linear hysteresis motors.

The levitation of our linear stage uses a novel magnetic design, where the suspension of the stage in three DOFs, including vertical, pitch, and roll, is achieved passively through the PM bias magnetic flux. Such compact magnetic design effectively reduces the number of sensors and actuators required for stabilizing the stage's levitation. This configuration resembles that of bearingless slice motors [14], where the rotors are typically in thin disk shape. With the magnetic field on the rotor's peripheral, such a slice rotor can be passively suspended in the axial-, tip-, and tilt-directions. Prior work on various designs of rotary bearingless slice motors includes [15]–[17]. To our knowledge, our work presents the first linear bearingless slice motor design.

The operating principle, hardware design, and preliminary tests of our linear stage have been presented in our recent conference papers [18] and [19]. This paper further introduces the stage's magnetic modeling and feedback control system, and presents further experimental results for performance evaluation.

The rest of this paper is organized as follows: Section II presents the operating principle of our magnetically-levitated linear stage. Section III introduces the hardware of the prototype. Section IV presents the magnetic modeling for the linear stage. Section V discusses the feedback control system design. Section VI presents the

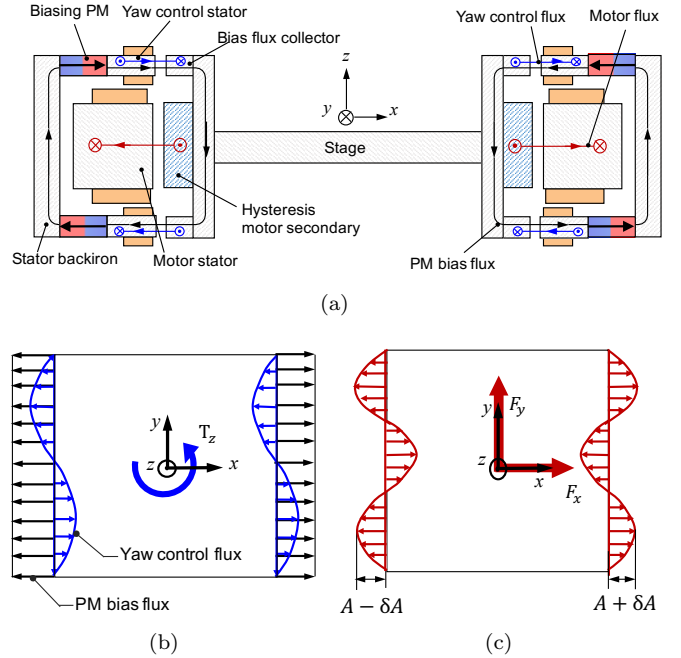


Fig. 2. Magnetic fluxes and the suspension forces/torques generation in the magnetically-levitated linear stage. (a) Cross-section diagram of the stage. (b) Top view of the PM bias fluxes (black) and the yaw-control fluxes (blue) in the air gaps. (c) Top view of the motor fluxes (red) in the air gaps.

experimental tests. Conclusions and suggested future work are presented in Section VII.

II. OPERATING PRINCIPLE

Figure 1 shows a cross-section CAD model and a photograph of the hysteresis-motor-driven magnetically-levitated linear stage, which comprising two stator assemblies, one moving stage, and a sensing system. Figure 1 also shows the coordinate system. The translation of the moving stage is along the y -axis. The stage's magnetic levitation is actively controlled in the x - and θ_z -DOFs, and is passively stabilized in the z -, θ_x -, and θ_y -DOFs. When the linear stage is used for in-vacuum reticle transportation, a channel made of thin walls (not shown in figures) needs to be configured surrounding the stage's motion range. The moving stage is magnetically suspended and transports the reticle in clean vacuum inside the channel, while the stator assemblies are arranged out of the channel, and are in a vacuum environment with less tight contamination control. This channel is thus able to separate out the contamination generation from the stator assemblies.

Our stage uses a linear bearingless slice motor design, where flux-biased magnetic bearings and linear hysteresis motors are combined. We next discuss the suspension forces/torques generation mechanisms in the linear stage. Following this we discuss the thrust force generation mechanism for linear hysteresis motors.

A. Suspension Forces/Torques Generation

Figure 2a shows a cross-section diagram of the magnetic structure for our linear stage system including the mag-

netic fluxes, and Fig. 2b and Fig. 2c show the top views of magnetic fluxes in the bias flux air gaps and the motor flux air gaps, respectively. As shown in Fig. 2a, the stator assemblies include two kinds of stators: the motor stators are interfacing with the hysteresis secondaries on the moving stage, and the yaw-control stators are interfacing with the bias flux collectors. Four rows of biasing PMs are arranged on the back of the yaw-control stators, and the top and bottom biasing magnets are connected via a stator backiron in each stator assembly.

There are three magnetic fluxes in our linear stage system. The black flux lines in Fig. 2a and Fig. 2b show the PM bias magnetic fluxes generated by the magnets in the stator assemblies. Such air gap bias fluxes can generate passive suspension force/torque in the z -, θ_x -, and θ_y -DOFs. When the stage has motion in these directions, the bias air gap fluxes are tilted and therefore generate restoring force and torques, and thereby stabilize the magnetic suspension passively. Note that the PM bias fluxes also generate destabilizing force/torque in the x - and θ_z -directions, and feedback control is thus needed to stabilize the stage's magnetic suspension in these DOFs.

The blue flux lines in Fig. 2a and Fig. 2b represent the yaw-control fluxes, which are produced by the yaw-control stators. The yaw-control flux is distributed approximately sinusoidally in the air gaps, and is synchronous with respect to the moving stage. This flux steers the air gap bias magnetic flux (black flux lines) for yaw (θ_z) suspension control torque generation. For example, in Fig. 2b, the yaw-control flux weakens the PM bias flux in top right and bottom left areas, while strengthens the flux in bottom right and top left areas, thereby generating a yaw-controlling torque about the z -axis as shown in Fig. 2b.

The red flux lines in Fig. 2a and Fig. 2c show the motor fluxes, which are produced by the motor stators on the left and right of the moving stage. The common-mode of the two motor fluxes generates y -directional thrust force on the moving stage through interacting with the linear hysteresis motor secondaries. The differential of the two motor fluxes generates lateral-directional reluctance forces, which actively controls the stage's levitation in the x -direction. With all three magnetic fluxes, we are able to stabilize all five suspension DOFs of the moving stage, either actively or passively.

B. Thrust Force Generation

Our linear stage's thrust force generation uses short-secondary linear hysteresis motors. Hysteresis motors have secondaries made of magnetically semi-hard materials. When the motor's stator is excited, the secondary material's hysteresis effect generates a spatial lag between the secondary magnetization and the external field, and thus generates thrust force [12]. The hysteresis secondaries are often pre-magnetized using a large stator current amplitude pulse to improve the motor's thrust generation capability [20]. Recent work [21] studied the effect of such pre-magnetization for rotary hysteresis motors.

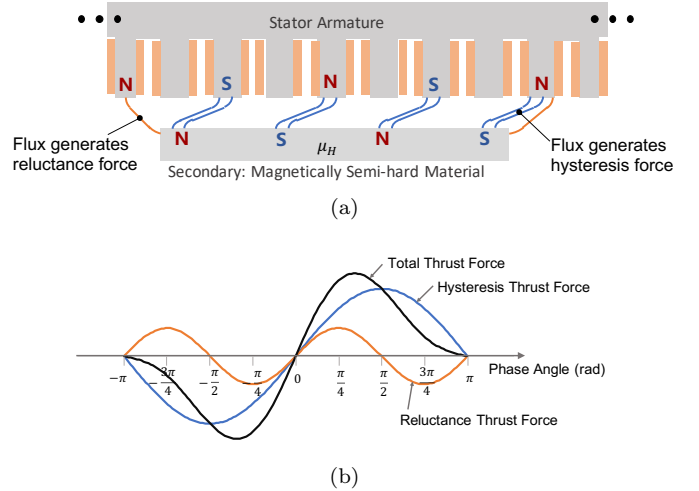


Fig. 3. (a) Air gap magnetic flux diagram in a linear hysteresis motor. (b) Diagram of thrust force and stator current phase relationship in a linear hysteresis motor.

In a linear hysteresis motor, aside from the hysteresis thrust forces, additional y -directional reluctance forces are generated at the front and back edges of the hysteresis motor secondaries. Such motor behavior is called the end effect. Figure 3a shows an air gap flux diagram for a linear hysteresis motor, where the blue flux lines generate the hysteresis thrust force, and the orange flux lines at the front and back edges of the secondary generate the reluctance thrust force. Figure 3b shows a diagram of the thrust force versus phase relationship of a linear hysteresis motor in synchronous operation. In this diagram, the horizontal axis represents the phase difference between the stator current and the secondary's position. Note that the hysteresis thrust force (blue line) has its peak values at phase angles of $\pm\pi/2$, while the reluctance force (orange line) has two periods in $-\pi$ to π . The summation of the two forces makes the phase of the peak total thrust force shift to the center, as shown by the black line in Fig. 3b.

Hysteresis motors can operate in either synchronous or asynchronous mode. In our system, we operate the linear hysteresis motors synchronously for two reasons: First, the end-effect reluctance forces are oscillatory if the motor is driven asynchronously, which can generate an undesirable vibration. Second, synchronous running of the motors eliminates eddy current and hysteresis losses in the secondaries generated by the fundamental harmonic field interactions. This is especially important for in-vacuum operation, since the in-vacuum cooling of the moving stage is challenging due to the absent of conduction and convection heat transfer.

III. HARDWARE OVERVIEW

We have built a magnetically-levitated linear stage prototype as shown in Fig. 1b. This section presents an overview of the hardware prototype, including the moving stage, the stator assemblies, and the sensing system. The values of the key design parameters are shown in Table I.

TABLE I
KEY DESIGN PARAMETERS

Variable	Parameter	Value
m_{ms}	Moving stage mass	4.8 kg
l_{ms}	Moving stage total length	192 mm
w_{ms}	Moving stage width	219 mm
h_{ms}	Moving stage height	74.7 mm
w_H	Hysteresis secondary width	40 mm
h_H	Hysteresis secondary thickness	9.53 mm
g_m	Motor flux air gap length	1.5 mm
g_b	Bias flux air gap length	2 mm
g_{mech}	Mechanical air gap length	0.5 mm
B_{bias}	Bias magnetic flux density	0.45 T
Δ_{sag}	Vertical sag due to stage's weight	0.75 mm

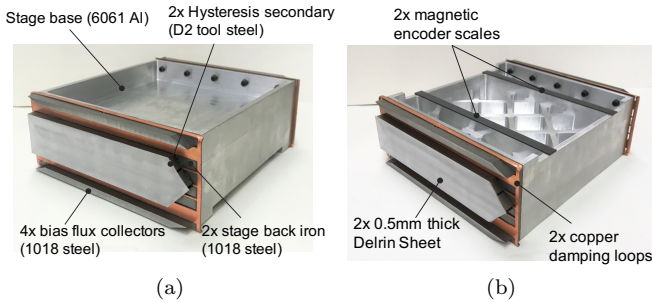


Fig. 4. Photographs of the moving stage. (a) Top view. (b) Bottom view.

TABLE II

Material	Recoil permeability μ_r	Coercivity H_c
D2 tool steel	29	7 kA/m
CROVAC 12	19	20 kA/m
AlNiCo 2	5.6	44 kA/m
AlNiCo 5	5.2	48 kA/m

A. Moving Stage

Figure 4 shows the photos of the moving stage, which comprises an aluminum stage base, two stage back-irons, two hysteresis motor secondaries, four bias flux collectors, two copper damping plates, and two optical sensor target sheets. The hysteresis motor secondaries and the bias flux collectors are all having skewed edges to reduce the tooth harmonic force generation on the moving stage. The hysteresis motor secondary material uses D2 tool steel hardened to 65 RC. Table II shows the magnetic properties of typical secondary materials for hysteresis motors. Although materials with larger magnetic hysteresis exist, D2 tool steel is selected here since its magnetic permeability is relatively large, which is advantageous for reluctance force generation for magnetic suspension purpose. Figure 5 shows the measured B - H curves of hardened D2 steel under varying excitation amplitude. The initial magnetization curve is defined by the maximum points of all loops, as shown by the red circles.

Copper damping plates with conductive loops are configured around the secondaries to improve the stage's damping in the passively-levitated directions: when the stage is having velocity in these directions, eddy currents

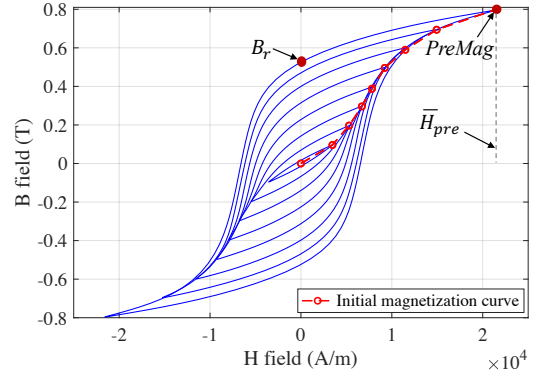


Fig. 5. Measured hysteresis property of D2 tool steel under varying excitation amplitude. \bar{H}_{pre} : maximum field intensity during pre-magnetization phase. B_r : remanence of secondary after pre-magnetization.

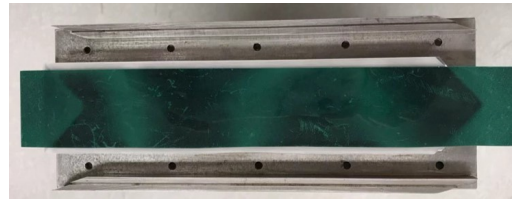


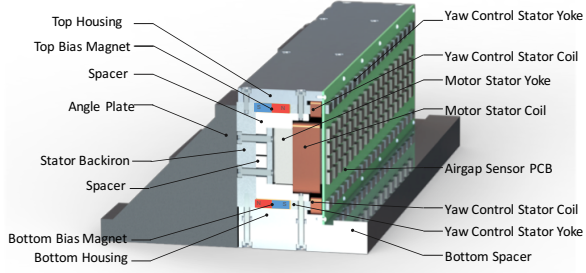
Fig. 6. Photograph of the pre-magnetized hysteresis secondary under a magnetic viewing film.

can be induced in the loops of the copper plates, and thus damp the stage's motion. The thickness of the copper plates is 0.5 mm. The damping performance with and without the copper plates are presented in Section VI-A.

In our linear stage, the hysteresis secondaries are pre-magnetized to improve the motors' thrust force generation capability. The pre-magnetization of the secondaries is achieved by setting the corresponding air gap to zero, i.e. putting the hysteresis secondary in full contact with the motor stator, and gradually increasing the stator's current amplitude up to 5 A. The hysteresis secondaries on both sides of the stage are magnetized symmetrically in this manner. Figure 6 shows a photo of the pre-magnetized stage secondary under a magnetic viewing film, where the arrow-shaped hysteresis secondary shows a periodical magnetization pattern. When the system is in operation, the stator's current amplitude is limited below 2.5 A, and the motor air gap length is 1.5 mm. At this time, the stator-generated field intensity is significantly lower than that in the pre-magnetization phase, which does not change the magnetization status of the secondaries.

B. Stator Assembly

Figure 7a shows a cross-section CAD model for the stator assembly, and Fig. 7b shows a front-view photograph of the stator assembly with the air-gap sensor printed circuit board (PCB) removed. The stator assembly primarily consists of one motor stator, two yaw-control stators, and a flux-biasing structure comprising one stator backiron and two rows of biasing PMs, as shown in Fig. 7a. The stator assemblies are fixed on the base optical table via three angle plates, as shown in Fig. 1b.



(a)



(b)

Fig. 7. (a) CAD model of the stator assembly. (b) Front-view photo of the stator assembly showing the winding patterns.

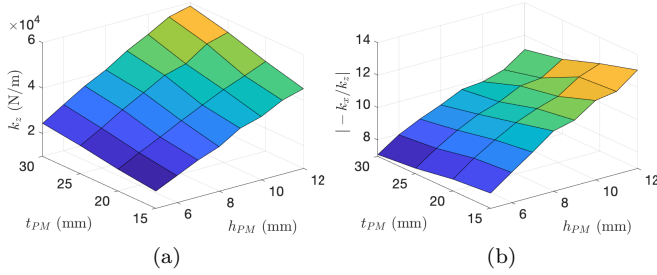


Fig. 8. Simulated flux bias structure performance with varying PM dimensions. t_{PM} : magnetization-directional dimension. h_{PM} : vertical-directional dimension. (a) Stage's passive stiffness in the vertical direction. (b) Ratio between x -DOF negative stiffness and z -DOF passive stiffness.

The most important design parameter of the flux-biasing structure is the dimension of the PMs, which determines the passive stiffness in the stable DOFs and the negative stiffness in the open-loop unstable DOFs. Figure 8 shows the stage's z -axis passive stiffness k_z and the ratio between x -axis negative stiffness and z -axis passive stiffness $|-k_x/k_z|$ under varying PM sizes simulated with 3D finite element method (FEM) using Ansys Maxwell. Here the bias flux air gap length is 2 mm. It can be observed in Fig. 8 that the passive stiffness k_z increases as t_{PM} and h_{PM} increase, while minimizing $|-k_x/k_z|$ requires a large t_{PM} and small h_{PM} . Our design goal is to minimize $|-k_x/k_z|$ while satisfying $k_z \geq 2 \times 10^4$ N/m, which provides a natural frequency of as least 10 Hz in the z -direction. In the prototype system, we selected $t_{PM} = 25.4$ mm (1 inch) and $h_{PM} = 6.35$ mm (1/4 inch), which is close to the optimal design, and PMs with such dimension are available off-the-shelf. With this design, the air gap bias flux density is 0.45 T, and the sag due to the stage's weight is 0.75 mm.

Tooth wound winding is selected for both the motor

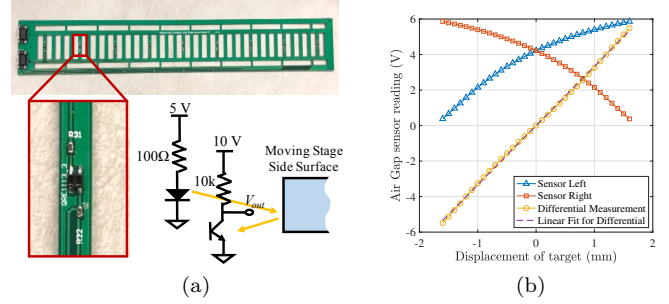


Fig. 9. Optical air gap sensors. (a) Photo of the air-gap sensor PCB (QRE1113GR from On Semiconductor) and the circuit diagram. (b) Calibration data of the reflective optical air-gap sensors.

stators and the yaw-control stators mainly due to its advantage of short end winding, which allows the stator assembly to fit in the height limit of the reticle handling system (100 mm). Figure 7b shows the winding patterns of the motor stator and the yaw-control stators. The motor stator has three-phase windings U , V , and W wound on the stator teeth. Here $-U$ indicates a coil in the same phase with U , while its current is in a reversed direction. In the motor stator, one full period consists of six stator teeth, with the winding pattern being $(U, -W, V, -U, W, -V)$. The hysteresis secondary length equals nine stator tooth pitch, which is 1.5 times of the stator wavelength. The yaw-control stators have five-phase windings, where one full period has 10 stator teeth in a winding pattern $(A, -D, B, -E, C, -A, D, -B, E, -C)$. All the corresponding phases in all four yaw-control stators are connected in series.

In our system, the magnetic air gap between the hysteresis secondary and the motor stators is 1.5 mm, and the magnetic air gap for the bias flux path is 2 mm. To mimic the separation wall between stator and the moving stage, we attached a 0.5 mm-thick plastic shim on the pole face of each motor stator, and an additional 0.5 mm-thick Delrin sheet is attached on each hysteresis secondary as the optical sensor target. As a result, the linear stage has a mechanical air gap length of 0.5 mm on both sides.

C. Sensing System

Two kinds of sensors are used to measure the stage's displacement in the x -, y -, and θ_z -DOFs, including the optical reflective sensors and the magnetic encoders.

To measure the stage's motion in the x - and θ_z -DOFs at different y -positions, 18 reflective-type optical displacement sensors (QRE1113GR from On Semiconductor Inc.) are arranged along the y -direction on two PCBs, and the PCBs are mounted on the front-directional surfaces of the two stator assemblies. With this configuration, there are two optical sensors placed in opposition at the same y -directional position to measure the stage's lateral displacement differentially. Figure 9a shows a photo of the optical sensor PCB and a schematic diagram of the optical sensor's circuit. The sensor consists of an infrared LED and a phototransistor facing the same direction. As

shown in Fig. 9a, the LED shines an infrared beam on the side surface of the moving stage, and the phototransistor detects the reflected light. Two 0.5 mm-thick white Delrin sheets are epoxied on the side surfaces of the moving stage serving as the optical sensor targets, as shown in Fig. 4. Figure 9b shows the calibration data of the optical sensors with respect to the stage's x -displacement. Data show that the differential signal of left and right optical sensor outputs is largely linear with respect to the lateral displacement of the moving stage.

The stage's y -directional position is measured by dual linear magnetic encoders. In order to achieve a design where no cable is attached to the moving stage, two magnetic encoder scales are arranged on the bottom surface of the moving stage, as shown in Fig. 4b. Two rows of encoder readheads (LM15 from Renishaw Inc), with four encoder readheads per row, are configured along the moving direction of the stage, as shown in Fig. 1. The moving stage's y -directional position signal is synthesized from the encoder readings by integrating the increment of the encoder reading from the readhead that is engaged with the stage. The resolution of the encoders is 1.2 μm . Note that the magnetic encoder scales are not vacuum compatible. When the system needs to operate in vacuum, an alternative displacement sensor is needed, for example using laser interferometers.

IV. LINEAR STAGE MODELING

This section presents the magnetic modeling of our linear stage system, including: (a) an FEM-based model for the pre-magnetized linear hysteresis motors, and (b) an analytical model for the stage's suspension controlling force/torque in the x - and θ_z -DOFs.

A. Pre-magnetized Linear Hysteresis Motor Modeling

The modeling of the pre-magnetized linear hysteresis motors uses numerical simulations, since the material's hysteresis property is highly nonlinear and thus difficult to model analytically. Here the finite element package FEMM [22] is used. The modeling process takes three steps as introduced in the following.

1) *Step I: Pre-magnetizing field calculation:* We first calculate the motor's field intensity (H -field) distribution generated by the stator in the pre-magnetization process. In this simulation, the motor air gap length is set to zero, and the stator current amplitude is 5 A. The secondary material is defined via the initial magnetization curve of the D2 steel as shown by red circles in Fig. 5. Fig. 10a shows the simulated H -field distribution in the linear hysteresis motor in the pre-magnetization process. A stage-fixed coordinate x_r - y_r is defined as shown in Fig. 10a, and a line AA' is defined as a horizontal line in the secondary through the middle of its thickness. Figure 10b and Fig. 10c show the magnitude and angle of the simulated H -field along line AA' . Considering only the fundamental harmonic of the H -field in the secondary, we take the average magnitude \bar{H}_{pre} and the linear fit

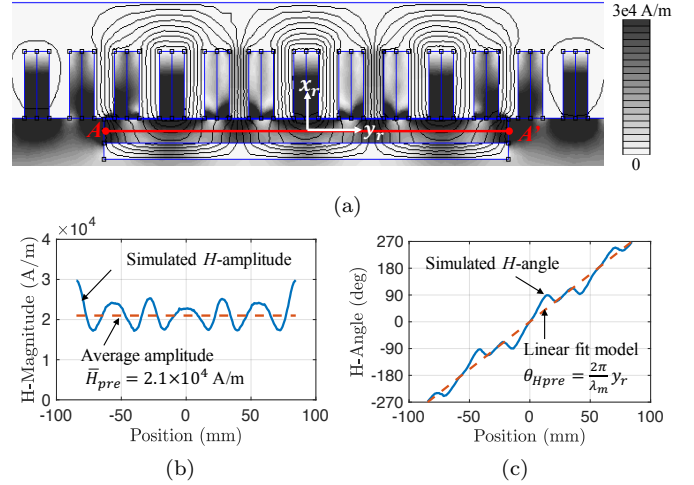


Fig. 10. Hysteresis secondary pre-magnetization process simulation (step I). (a) Field intensity (H -field) simulated with FEM. (b) H -field magnitude along line AA' . (c) H -field angle along line AA' .

of the angle θ_{Hpre} to model the pre-magnetizing field, as shown by the dashed lines in Fig. 10b and Fig. 10c. Here $\bar{H}_{pre} = 2.1 \times 10^4$ A/m and $\theta_{Hpre} = 2\pi y_r / \lambda_m$, where λ_m is the wavelength of the motor stator winding. Note that this model ignores the tooth harmonics of the pre-magnetizing field, and thus it only predicts the average thrust force generation of the linear hysteresis motors.

2) *Step II: Checking B-H data:* We next use the calculated average magnetizing field \bar{H}_{pre} to determine the secondary material property after the pre-magnetization. As shown in the measured D2 tool steel hysteresis data in Fig. 5, the value \bar{H}_{pre} is shown by the vertical line labeled \bar{H}_{pre} , and the corresponding material property is represented the point *PreMag*. When the external pre-magnetizing field is removed, the material property can be represented by the point labeled B_r in Fig. 5, and the remanence is $B_r = 0.53$ T. The material's permeability after the pre-magnetization is the slope of the B - H curve at the B_r point, i.e. $\mu_H = 29\mu_0$.

3) *Step III: Thrust force calculation:* Finally, the pre-magnetized D2 tool steel secondary is modeled as a PM array, and the motor thrust force is calculated via FEM. Figure 11a shows a diagram of the FEM model for thrust force calculation. Here, the pre-magnetized hysteresis secondary is modeled as an array of PMs comprising 40 segments. The material remanence and permeability of the PM segments are $B_r = 0.53$ T and $\mu_H = 29\mu_0$, respectively. The magnetization direction of each PM segment is determined by the pre-magnetizing H -field direction, i.e. $\theta_{Hpre} = 2\pi y_r / \lambda_m$. Note that here we assumed linear material property for the hysteresis secondary after the pre-magnetization. This assumption is acceptable for our linear stage since the field intensity during the motor's operation is significantly lower than that during the pre-magnetization phase. Figure 11b shows the FEM simulated flux density distribution in one linear hysteresis motor. Note that here the calculated thrust force includes both hysteresis and reluctance force, since the secondary material has magnetization for hysteresis force generation,

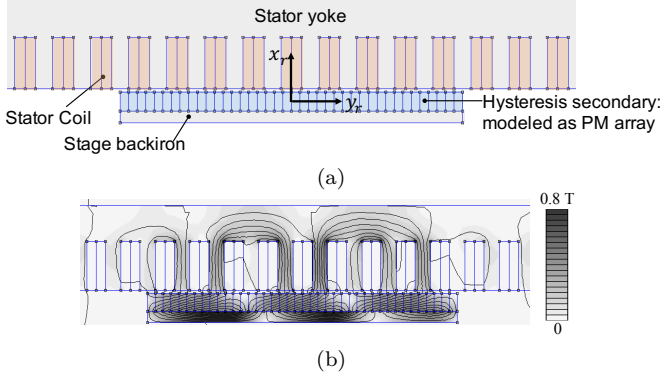


Fig. 11. Thrust force calculation for the pre-magnetized linear hysteresis motor via FEM (step III). (a) FEM model diagram. (b) Simulated B -field distribution in motor at 2 A current amplitude.

and also has a relatively high permeability for reluctance force generation. The simulated thrust force of the linear motor is compared with the experimental measurements in Section VI-B.

B. Levitation Controlling Force/Torque Modeling

This section presents an analytical model for the stage's suspension control force and torque in the x - and θ_z -directions. The assumptions of the model include: (a) The stage is assumed to be centered in between the two stator assemblies. (b) Only the fundamental harmonic of the stator and secondary magneto-motive forces (MMFs) are considered. (c) Flux concentration at the front and back of the stage, i.e. the end effect, is ignored. (d) The stator yokes, stage backiron, and bias flux collectors are assumed to be infinitely permeable. (e) Only the normal-directional air gap fluxes are considered.

C. Lateral Suspension Force Generation

We first discuss the x -directional suspension control force generation between the motor stators and the hysteresis secondaries. The fundamental harmonic MMF of the pre-magnetized hysteresis secondary is

$$\mathcal{F}_H = \frac{B_r}{\mu_H} h_H \cos\left(\frac{2\pi}{\lambda_m} y_r\right), \quad (1)$$

where y_r is the y -directional position in the stage-fixed coordinate, h_H is the hysteresis secondary thickness, λ_m is the motor winding wavelength, B_r and μ_H are the remanance and permeability of the pre-magnetized hysteresis secondary, respectively, which are found in Section IV-A.

The fundamental harmonic MMF generated the left and right motor stator windings are

$$\mathcal{F}_m^L = N_m I_m^L \cos(2\pi y_r / \lambda_m + \phi_m), \quad (2)$$

$$\mathcal{F}_m^R = N_m I_m^R \cos(2\pi y_r / \lambda_m + \phi_m), \quad (3)$$

where N_m is the equivalent number of turns per pole for the motor stator winding, I_m^L and I_m^R are the current amplitudes of the left and right motor stators, respectively, ϕ_m is the spatial phase difference between the motor stator excitation and the moving stage's position.

The total permanence of the motor air gap and the hysteresis secondary layer can be calculated as

$$P_{gm} = \mu_0 / g_{eq}, \quad (4)$$

where μ_0 is the vacuum permeability. $g_{eq} = g_m + h_H \frac{\mu_0}{\mu_H}$ is the equivalent air gap length of the motor with the effect of hysteresis secondary taken into account, where g_m is the motor flux air gap length. Then the normal-directional flux distribution in the two motor air gaps are

$$B_m^L = P_{gm}(\mathcal{F}_m^L + \mathcal{F}_H), \quad B_m^R = P_{gm}(\mathcal{F}_m^R + \mathcal{F}_H). \quad (5)$$

The total x -directional reluctance force on the stage generated by the motor stators can be calculated using the Maxwell stress tensor method as

$$f_m^x = \int_{-L_H/2}^{L_H/2} \frac{B_m^{R2} - B_m^{L2}}{2\mu_0} w_H dy_r, \quad (6)$$

where L_H and w_H are the length and width of the hysteresis motor secondary, respectively, and $L_H = 1.5\lambda_m$ for our linear stage. Substituting (1)-(5) into (6), we have

$$f_m^x = \frac{3\mu_0 \lambda_m w_H}{4g_{eq}} \left((N_s^2 I_m^{R2} + N_s I_m^R \frac{B_r}{\mu_H} h_H \cos \phi_m) - (N_s^2 I_m^{L2} + N_s I_m^L \frac{B_r}{\mu_H} h_H \cos \phi_m) \right). \quad (7)$$

Define $I_{bias} = (I_m^L + I_m^R)/2$ and $\delta I_m = (I_m^R - I_m^L)/2$ as the common-mode and differential current amplitudes of the left and right motor stators, respectively. Therefore we have $I_m^R = I_{bias} + \delta I_m$, $I_m^L = I_{bias} - \delta I_m$. Then the stage's total x -directional force in (7) can be calculated as

$$f_m^x = \frac{3\mu_0 \lambda_m w_H}{2g_{eq}} (2N_s^2 I_{bias} + N_s \frac{B_r}{\mu_H} h_H \cos \phi_m) \delta I_m. \quad (8)$$

When the linear stage is operating, I_{bias} is set to a constant value for thrust force generation, and δI_m is used to control the stage's suspension in the x -direction. Define the coefficient in front of δI_m in (8) as K_i^x , which is the force constant for the stage's x -directional magnetic suspension. Then (8) can be written as

$$f_m^x = K_i^x \delta I_m. \quad (9)$$

Figure 12a shows the analytically calculated x -directional reluctance force plotted together with the FEM simulation result. Good agreement between the two simulation results validates the analytical model.

D. Yaw Suspension Torque Generation

This section models the θ_z -directional suspension torque generation using a combination of the PM bias flux and the yaw-control stator excitation. The MMF generated by one yaw-control stator is

$$\mathcal{F}_s = N_s I_s \sin\left(\frac{2\pi}{\lambda_s} y_r\right), \quad (10)$$

where N_s is the equivalent number of turns per pole of the yaw-control stator, I_s is the current amplitude in the

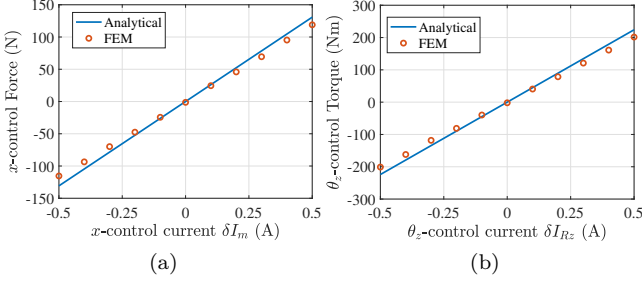


Fig. 12. Comparison between analytically calculated suspension control force/torque and FEM simulation results. (a) x -axis control force at $I_{bias} = 2$ A and $\phi_m = 0$ rad. (b) θ_z -axis control torque.

yaw-control stator windings, and λ_s is the wavelength of the yaw-control stator winding.

Note that the yaw-control flux shares the same air gap with the PM bias flux, as shown in Fig. 2b. The bias flux air gap permeance is

$$P_{gs} = \mu_0/g_b, \quad (11)$$

where g_b is the bias flux air gap length. Assume the PM bias flux is uniformly distributed in all bias flux air gaps with an amplitude of B_{bias} . The magnetic flux distribution in one bias flux air gap is

$$B_s = B_{bias} + P_{gs}\mathcal{F}_s = B_{bias} + \frac{\mu_0}{g_b}N_s I_s \sin\left(\frac{2\pi}{\lambda_s}y_r\right). \quad (12)$$

The normal-directional force and θ_z -directional torque generated in this air gap are

$$F_s^n = \int_{-\frac{L_b}{2}}^{\frac{L_b}{2}} \frac{B_s^2 w_b}{2\mu_0} dy_r = \frac{w_b \lambda_s B_{bias}^2}{2\mu_0} + \frac{w_b \mu_0 \lambda_s N_s^2 I_s^2}{4g_b^2}, \quad (13)$$

$$T_s = \int_{-\frac{L_b}{2}}^{\frac{L_b}{2}} \frac{B_s^2 w_b}{2\mu_0} y_r dy_r = \frac{N_s w_b \lambda_s^2 B_{bias} I_s}{2\pi g_b}, \quad (14)$$

where L_b and w_b are the length and width of the bias flux collector, respectively, and $L_b = \lambda_s$. In our linear stage, all four yaw-control stators share the same current amplitude I_s . The normal-directional attractive forces F_s^n cancel out when the stage is centered, and the total controlling torque on the stage about the vertical axis is $T_s^z = 4T_s$. Define $K_i^{Rz} = (2N_s w_b \lambda_s^2 B_{bias})/(\pi g_b)$. Then the total yaw-directional torque on the moving stage is

$$T_s^z = K_i^{Rz} I_s. \quad (15)$$

Figure 12b shows a comparison between the modeled θ_z -directional controlling torque and the FEM simulation result. It can be seen that the model and FEM results are matching well, which validates our model for the θ_z -DOF torque generation.

V. FEEDBACK CONTROL SYSTEM

Figure 13 shows a control block diagram for our magnetically-levitated linear stage prototype. Here, the x - and θ_z -directional displacements of the stage are estimated from the optical sensor and magnetic encoder measurements as \hat{x} and $\hat{\theta}_z$, and are fed back for suspension

TABLE III
CONTROLLER PARAMETERS

DOF	K_p	T_i [ms]	α	τ [ms]	T_f [ms]
$C_x(s)$	0.8 A/mm	8	10	0.7	0.4
$C_{\theta_z}(s)$	2.2 A/deg	10	10	0.8	0.4
$C_y(s)$	12 rad/mm	10	10	1.6	0.5

control. For more details about the stage displacement estimation method see [23]. The x -directional error signal e_x is amplified by the x -DOF suspension controller $C_x(s)$, and the control effort signal u_x is used as the differential of the left and right motor current amplitudes, i.e. δI_m in (9). In addition to u_x , a constant bias current I_{bias} is injected to the motor stators' current amplitude for maintaining magnetic suspension and for thrust force generation. The value of $|u_x|$ is typically small when the linear stage is in operation, and $I_{bias} \gg |u_x|$. As a result, the influence of u_x to the stage's y -directional force generation is small and therefore assumed negligible.

The linear hysteresis motors are operated synchronously in the linear stage system. The y -directional position control loop for the stage is closed with the encoder signal y_{meas} being used for feedback. The y -DOF control effort signal u_y is used as the phase difference between the motor stator excitation and the moving stage, i.e. ϕ_m in (2), (3) and (8). Therefore the phase of the motor stator currents is $\phi_{motor} = \frac{2\pi}{\lambda_m} y_{meas} + u_y$. The value of u_y is limited within $[-\frac{\pi}{4}, \frac{\pi}{4}]$ since the stage's thrust force is largely linear with respect to u_y in this range. This also limits the variation of K_i^x value within 5% during the stage's operation, which allows us to use constant gains in the x -DOF suspension controller. With the amplitude and phase of the motor currents determined, the current commands for the left and right motor stator windings can be calculated with three-phase distributors. These signals are then sent out to current-controlled power amplifiers and energize the motor stators.

The estimated yaw displacement $\hat{\theta}_z$ is injected into the yaw suspension controller $C_{\theta_z}(s)$, and the control effort signal u_{θ_z} is used to determine the yaw-control stators' current amplitude, i.e. I_s in (15). The yaw-control stator excitation is synchronous with the moving stage, with its phase being $\phi_{yaw} = \frac{2\pi}{\lambda_s} y_{meas}$. The yaw-control currents are calculated by a five-phase distributor, and are sent out to the power amplifiers to energize the yaw-control stators.

The suspension and motion controllers in Fig. 13 implement lead-lag controllers with high-frequency roll-off as

$$C(s) = K_p \left(1 + \frac{1}{T_i s}\right) \frac{\alpha \tau s + 1}{\tau s + 1} \cdot \frac{1}{T_f s + 1}, \quad (16)$$

where K_p is the proportional gain, T_i is the integral time constant, α is the lead controller constant, τ is the lead time constant, and T_f is the low pass filter time constant. The controller design uses the loop shaping method, and Table III shows the parameters for the three controllers in Fig. 13. The control performance of the linear stage prototype is presented in Section VI.

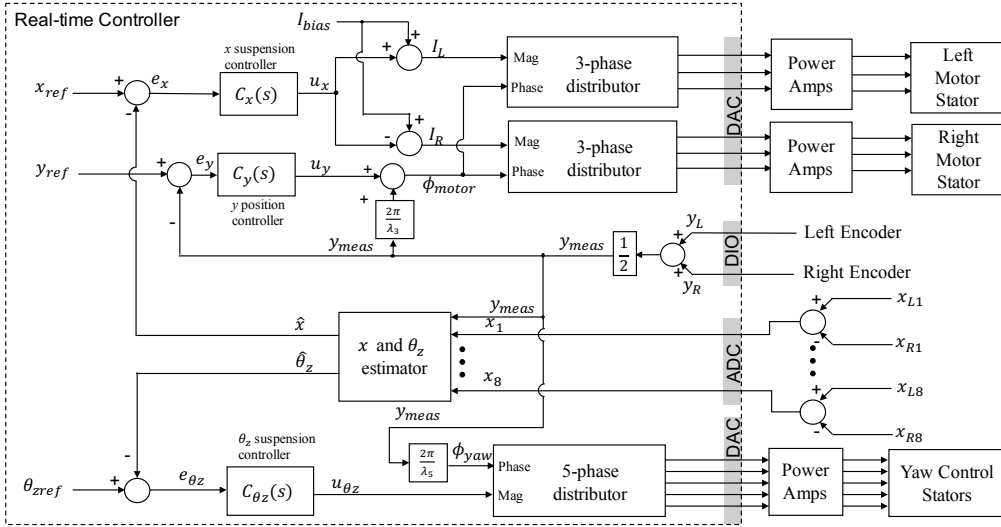


Fig. 13. Control system block diagram of the magnetically-levitated linear stage prototype.

TABLE IV

MEASURED PASSIVE LEVITATION PERFORMANCE UNDER $I_{bias} = 2$ A.

DOF	Res. Freq.	Pass. Stiffness	Damping w/o Cu plate	Damping w/ Cu plate
z	12.9 Hz	310 kN/m	0.07	0.1
θ_x	10.6 Hz	76 Nm/rad	0.012	0.018
θ_y	9.1 Hz	118 Nm/rad	0.022	0.03

The control algorithm shown in Fig. 13 is implemented in a realtime controller NI 8108 with FPGA modules via LabVIEW programming language. The control loop runs at a sampling rate of 5 kHz. For further implementation details of the control system see [23].

VI. EXPERIMENTS

A. Suspension Tests

When the power is off, the moving stage touches on one of the stator assemblies on the side due to the negative stiffness caused by the PM bias fluxes. The stage's maximum off-centering displacement in the x -direction is 0.5 mm. As we turn on the power and the suspension controllers, the stage lifts off from the side wall and levitates at the center position between two stator assemblies.

Table IV presents the measured magnetic suspension performance of the stage in the passively-stabilized DOFs, including resonance frequency, passive stiffness, and damping ratio with and without the copper damping plates. Here, the resonance frequency and damping ratio are measured through the impulse responses of the stage in these modes, and the passive stiffness values are estimated via the measured natural frequencies and the stage's known inertia. Note that the stage's resonance frequency and damping are relatively low in the passive modes. This is mainly because our linear stage is operating at relatively large magnetic air gaps of 2 mm for the bias flux path and 1.5 mm for the motor flux path. These large air gap lengths are required for the inclusion of separation walls for contamination prevention. The stage sags 0.75 mm below

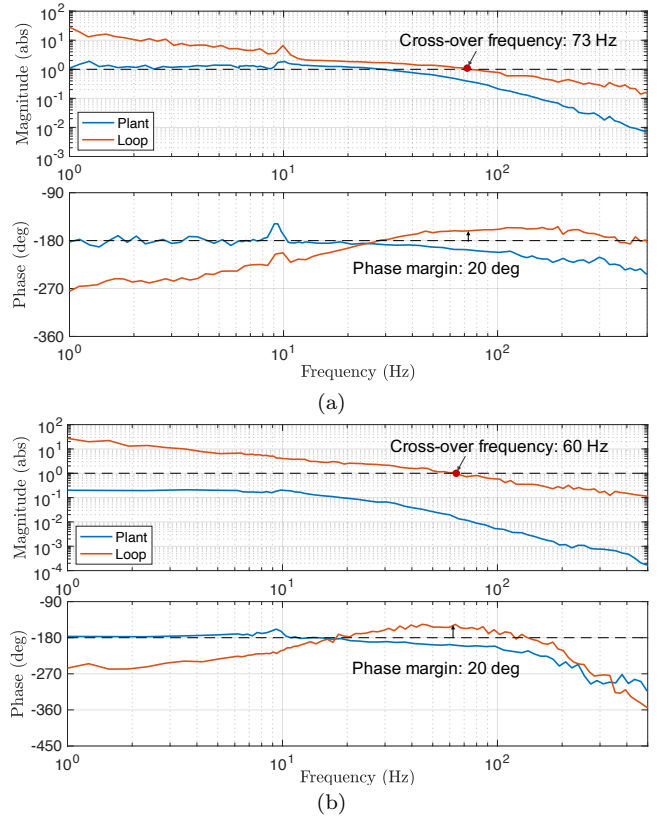


Fig. 14. Measured plant and loop frequency responses of the actively-controlled magnetic suspension of the linear stage. (a) x -DOF. (b) θ_z -DOF.

the equilibrium position in the vertical direction due to its weight.

The frequency responses of the stage's active magnetic suspension in the x - and θ_z -DOFs are measured and are shown in Fig. 14. Note that these measurements are taken with the stage's suspension control loops closed, since the systems are unstable in open-loop. In the x -DOF suspension plant Bode plot, the magnitude demonstrates a notch followed by a peak around 9 Hz, and the phase

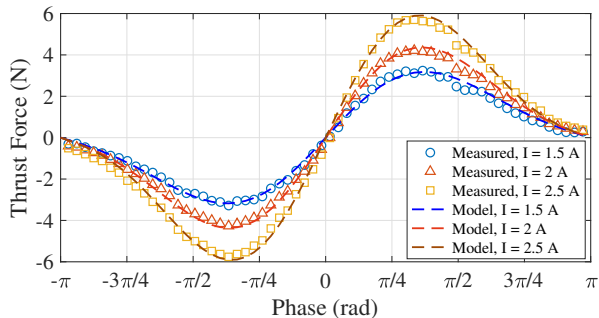


Fig. 15. Measured and modeled thrust force and phase relationship of the linear stage under different bias current amplitudes.

shows a peak at the same frequency, which indicates that complex zero- and pole-pairs are existing in the system dynamics. To our understanding, this is due to the second-order roll mode (θ_y -DOF) is added to the measured mode. Data show that the cross-over frequencies of the x - and θ_z -directional magnetic levitation are 73 Hz and 60 Hz, respectively, and the phase margin of both loops are around 20 degrees.

B. Linear Motor Tests

1) *Thrust Force Measurements*: The linear stage's thrust force is measured as a function of the phase difference between the stator excitation and the secondary magnetization. In this test, the moving stage is levitated in all DOFs and is fixed in the y -direction, and a force gauge is used to measure the thrust force while sweeping the phase of the motor stator currents. Figure 15 shows the measured thrust force and phase relationship of the linear stage under different bias current amplitudes. Note that the peak thrust force is generated when the phase angle is in between $\pm\pi/4$ and $\pm\pi/2$, which is due to the combination of hysteresis thrust force and reluctance thrust force as discussed in Section II-B. The simulated thrust force using the FEM-based linear hysteresis motor model introduced in Section IV-A is also plotted in Fig. 15 via dashed lines. Good agreement between the measured and simulated results validates our modeling process for the pre-magnetized linear hysteresis motors. The maximum thrust force of the linear stage is 5.8 N under 2.5 A bias current amplitude, which corresponds to a maximum stage acceleration of 1200 mm/s². This experiment shows that our linear stage prototype is able to satisfy the acceleration requirement of the reticle handling application (500 mm/s²).

2) *Closed-loop Position Control*: We closed the position control loop for the moving stage in the y -direction. Figure 16 shows the measured closed-loop step response of the y -directional position control of the moving stage. Here the 10%-90% rise time of the step response is 0.012 s, which corresponds to a position control bandwidth of 30 Hz. Figure 17 shows the measured tracking performance of the stage to a second-order polynomial reference trajectory, including the reference and measured position (top

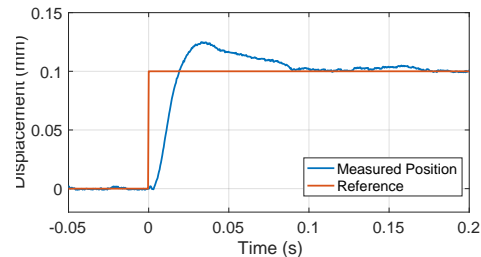


Fig. 16. Measured closed-loop position step response of the linear stage in the y -axis motion direction.

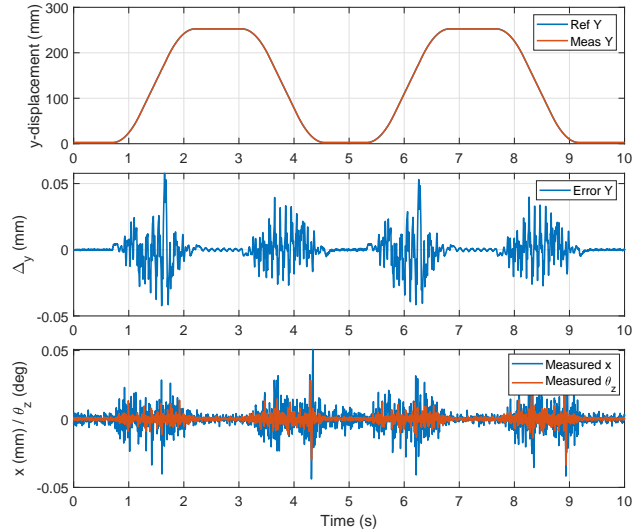


Fig. 17. Measured stage tracking performance to a second-order polynomial reference trajectory with $a_{max} = 500$ mm/s² and $v_{max} = 250$ mm/s. Top: reference and measured stage displacement. Middle: position tracking error. Bottom: measured stage displacements in x - and θ_z -directions.

plot), y -directional tracking error (middle plot), and the stage's x - and θ_z -directional displacements (bottom plot). The trajectory's maximum acceleration and velocity are 500 mm/s² and 250 mm/s, respectively. The middle plot in Fig. 17 shows that the maximum position control tracking error is about 50 μ m, and the tracking error demonstrates a periodic pattern, where the spatial period of the tracking error matches with the motor stator tooth pitch. To our understanding, this error is caused by the cogging force in the pre-magnetized linear hysteresis motors. The bottom plot in Fig. 17 shows that the stage's maximum deviation from center in the x -direction is about 50 μ m, which is well below making mechanical contact with the side walls (mechanical air gap length is 500 μ m on each side).

VII. CONCLUSIONS AND FUTURE WORK

In this paper, we have presented a novel magnetically-levitated linear stage driven by linear hysteresis motors. The moving stage uses secondaries made of vacuum-compatible magnetically semi-hard hysteresis alloy, which allows a simple moving stage construction. Passive magnetic suspension in three DOFs effectively reduces the number of actuators and sensors. The prototype system demonstrates a maximum acceleration of 1200 mm/s²,

and the maximum positioning error of the stage during transportation is 50 μm in both the motion and actively-suspended directions. The test results show that our linear motor prototype is able to successfully levitate the moving stage, and is able to satisfy the acceleration and position control requirements for the reticle transportation task.

Although satisfactory as a proof of concept, our linear stage design requires several improvements for being used in EUV lithography machines. (1) As discussed in Section VI-A, the stage's damping is relatively low in the passively-suspended DOFs. Future work should consider the design for additional dampers for the stage in the passively-levitated DOFs. (2) In our linear stage prototype, the optical air gap sensors cannot operate with opaque separation walls between the stage and the stators, and the magnetic encoder scales are not vacuum-compatible. Future work should design alternative vacuum-compatible displacement sensing system for the stage for the in-vacuum reticle transportation application.

ACKNOWLEDGMENT

The authors thank ASML for supporting this work. We thank Dr. Ruvinda Gunawardana and Dr. Minkyu Kim at ASML for the valuable discussions. We thank Dr. Alexander H. Slocum, Dr. Jeffery H. Lang, and Dr. James L. Kirtley at MIT for their constructive comments throughout the project. We thank Dr. Wolfgang Gruber and Dr. Gereon Goldbeck at JKU, Linz, Austria for their help with the hysteresis property measurements.

REFERENCES

- [1] C. Wagner and N. Harned, "Euv lithography: Lithography gets extreme," *Nature Photonics*, vol. 4, no. 1, p. 24, 2010.
- [2] D. L. Trumper, W.-j. Kim, and M. E. Williams, "Design and analysis framework for linear permanent-magnet machines," *IEEE Trans. Ind. Appl.*, vol. 32, no. 2, pp. 371–379, 1996.
- [3] H. Zhu, T. J. Teo, and C. K. Pang, "Design and modeling of a six-degree-of-freedom magnetically levitated positioner using square coils and 1-d halbach arrays," *TIA*, vol. 64, no. 1, pp. 440–450, 2016.
- [4] X. Lu *et al.*, "6d direct-drive technology for planar motion stages," *CIRP annals*, vol. 61, no. 1, pp. 359–362, 2012.
- [5] J. de Boeij, E. Lomonova, and A. Vandenput, "Modeling ironless permanent-magnet planar actuator structures," *IEEE Trans. Magnetics*, vol. 42, no. 8, pp. 2009–2016, 2006.
- [6] V. H. Nguyen and W.-j. Kim, "Two-phase lorentz coils and linear halbach array for multiaxis precision-positioning stages with magnetic levitation," *IEEE/ASME Trans. Mechatron.*, vol. 22, no. 6, pp. 2662–2672, 2017.
- [7] K. Sawada, "Outlook of the superconducting maglev," *Proceedings of the IEEE*, vol. 97, no. 11, pp. 1881–1885, 2009.
- [8] J. S. Choi and Y. S. Baek, "Magnetically-levitated steel-plate conveyance system using electromagnets and a linear induction motor," *IEEE Trans. Mag.*, vol. 44, no. 11, pp. 4171–4174, 2008.
- [9] T. Higuchi, "Linear stepping motor," Aug. 23 1988, US Patent 4,766,358.
- [10] Z. Sun, N. C. Cheung, J. Pan, S. Zhao, and W.-C. Gan, "Design and simulation of a magnetic levitated switched reluctance linear actuator system for high precision application," in *IEEE Int. Sym. Ind. Electron.* IEEE, 2008, pp. 624–629.
- [11] R. Grinham and A. Chew, "A review of outgassing and methods for its reduction," *Applied Science and Convergence Technology*, vol. 26, no. 5, pp. 95–109, 2017.
- [12] B. R. Teare, "Theory of hysteresis-motor torque," *Electrical Engineering*, vol. 59, no. 12, pp. 907–912, 1940.
- [13] L. Zhou, W. Gruber, and D. L. Trumper, "Position control for hysteresis motors: Transient-time model and field-oriented control," *IEEE Trans. Ind. Appl.*, vol. 54, no. 4, pp. 3197–3207, 2018.
- [14] R. Schoeb and N. Barletta, "Principle and application of a bearingless slice motor," *JSME Int. Journal Series C Mechanical Systems, Machine Elements and Manufacturing*, vol. 40, no. 4, pp. 593–598, 1997.
- [15] S. Silber, W. Amrhein, P. Bosch, R. Schob, and N. Barletta, "Design aspects of bearingless slice motors," *IEEE/ASME Trans. Mechatron.*, vol. 10, no. 6, pp. 611–617, 2005.
- [16] P. Puentener, M. Schuck, D. Steinert, T. Nussbaumer, and J. W. Kolar, "A 150 000-r/min bearingless slice motor," *IEEE/ASME Trans. Mechatron.*, vol. 23, no. 6, pp. 2963–2967, 2018.
- [17] M. Noh and D. L. Trumper, "Homopolar bearingless slice motor with flux-biasing halbach arrays," *IEEE Trans. Ind. Electron.*, vol. 67, no. 9, pp. 7757–7766, 2019.
- [18] L. Zhou and D. Trumper, "Magnetically levitated linear stage for in-vacuum transportation tasks," in *33rd ASPE Annual meeting*. ASPE, 2018, pp. 66–69.
- [19] J. Y. Yoon, L. Zhou, and D. L. Trumper, "Linear stages for next generation precision motion systems," in *IEEE/ASME Int. Conf. on Advanced Intelligent Mechatronics (AIM)*. IEEE, 2019, pp. 241–247.
- [20] M. A. Rahman and A. M. Osheiba, "Steady-state performance analysis of polyphase hysteresis-reluctance motors," *IEEE Trans. Ind. Appl.*, no. 3, pp. 659–663, 1985.
- [21] R. Galluzzi, N. Amati, and A. Tonoli, "Modeling, design and validation of magnetic hysteresis motors," *IEEE Trans. Ind. Electron.*, 2019.
- [22] D. Meeker, "Finite element method magnetics," FEMM, Tech. Rep., 2010.
- [23] L. Zhou, "Magnetically levitated hysteresis motor driven linear stage for in-vacuum transportation tasks," Ph.D. dissertation, Dept. of Mechanical Engineering, Massachusetts Institute of Technology, 2019.



Lei Zhou (S'15, M'19) received the B.E. degree in Control and Instrumentation Engineering from Tsinghua University, Beijing in 2012, and the S.M. and Ph.D. degrees in Mechanical Engineering from MIT in 2014 and 2019, respectively. She is currently an Assistant Professor with the Department of Mechanical Engineering at The University of Texas at Austin (UT Austin). Prior to joining UT Austin, she was a Visiting Research Scientist at the Mitsubishi Electric Research Laboratories for one year. Her research focuses on precision mechatronics, with an emphasis on electromagnetic design, actuators and sensors, precision control, and magnetic suspension.



David L. Trumper (M'90) joined the MIT Department of Mechanical Engineering in August 1993, and holds the rank of Professor. He received the B.S., M.S., and Ph.D. degrees from MIT in Electrical Engineering and Computer Science, in 1980, 1984, and 1990, respectively. Following the Bachelor's degree, Professor Trumper worked two years for the Hewlett-Packard Co. After finishing the Master's degree, he worked for two years for the Waters Chromatography Division of Millipore.

Upon completing the Ph.D. degree, for three years he was an Assistant Professor in the Electrical Engineering Department at the University of North Carolina at Charlotte, working within the precision engineering group. Professor Trumper's research centers on the design of precision mechatronic systems, with a focus on the design of novel mechanisms, actuators, sensors, and control systems. He has conducted research in topics including precision motion control, high-performance manufacturing equipment, novel measurement instruments, biomedical and bio-instrumentation devices, and high-precision magnetic suspensions and bearings. He is a member of the IEEE, ASME, and ASPE (past-President).